batteries

MDPI

Article

Sensitivity Analysis of Force Field Parameters in a Coarse-Grained Molecular Dynamics Slurry Model for Li-Ion Battery Electrodes

Merve Gençtürk [1,2,*] and Emre Biçer [3]

[1] Department of Chemical Engineering, Sivas University of Science and Technology, Sivas 58000, Türkiye
[2] Sivas Energy Storage Research and Application Center, Sivas University of Science and Technology, Sivas 58000, Türkiye
[3] Department of Chemistry, Faculty of Science, Ankara University, Ankara 06100, Türkiye; ebicer@ankara.edu.tr
* Correspondence: merve.gencturk@sivas.edu.tr

Abstract

Slurry mixing influences the electrode mesostructure and performance of Li-ion batteries. Coarse-grained molecular dynamics (CGMD) can model slurry behavior, but its predictions depend strongly on force-field (FF) parameters. This study presents a design of experiments (DOE)-based workflow to assess Lennard-Jones and Granular Hertz parameters in an $LiNi_{0.33}Mn_{0.33}Co_{0.33}O_2$ cathode slurry model containing 85 wt% active material and 15 wt% carbon–binder domain at a target slurry solid content of 46 wt%. Literature-based parameter sets yielded simulated densities of 1.064–1.931 g cm^{-3}. Fractional factorial screening identified the normal contact elastic constant (k_n) as the dominant density-controlling parameter, followed by the active-material interaction distance (σ_{AM}). DOE-guided optimization yielded a density of 1.407 g cm^{-3}, closer to the experimental value of 1.550 ± 0.002 g cm^{-3} than the baseline literature sets. The density-optimized parameters were independently evaluated using non-equilibrium molecular dynamics (NEMD) viscosity simulations. At 500 s^{-1}, the predicted steady-state viscosity deviated by 23.2% from experiment. At 65 s^{-1}, large internal stress fluctuations, box flipping, and atom loss prevented reliable viscosity estimation. The workflow provides a systematic, computationally efficient approach to FF parameter selection while identifying limitations of low-shear NEMD predictions.

Keywords: Li-ion batteries; electrode manufacturing process; electrode slurry; coarse-grained molecular dynamics (CGMD); force-field parameter selection; slurry rheology

Check for updates

Academic Editor: Zhenbo Wang

Received: 12 October 2026
Revised: 6 November 2026
Accepted: 9 November 2026
Published: 18 November 2026

Copyright: © 2026 by the authors. Licensee MDPI, Basel, Switzerland. This article is an open access article distributed under the terms and conditions of the Creative Commons Attribution (CC BY) license.

1. Introduction

Li-ion batteries (LIBs) have become the dominant energy-storage technology in the rapid transition toward renewable energy systems, driven by their critical roles in the electrification of the automotive sector, portable electronics, renewable energy integration and grid-scale storage applications [1]. The expanding deployment of LIBs across diverse applications has led to increasing performance requirements, particularly in terms of energy density and fast-charging capabilities [2,3]. To meet the increasing demands for high energy density and fast-charging capabilities, many studies have focused on the development of novel active material chemistries, electrolytes (including solid-state variants) and separator designs [4–6]. However, the electrochemical performance of these advanced materials is strongly influenced by the electrode mesostructure formed during manufacturing, which controls ion and electron transport pathways and reaction kinetics. Therefore, accurately

understanding and optimizing battery performance require a detailed characterization of the electrode mesostructure as formed during manufacturing [7]. Such an understanding allows Li^+ ion transport resistances to be minimized, resulting in enhanced overall power performance of the cell [8].

Among the various manufacturing steps, the slurry mixing process is an initial manufacturing step that directly affects the electrode slurry's homogeneity and stability. These characteristics, in turn, strongly affect the final electrode mesostructure. Although established procedures exist for the slurry mixing process in battery manufacturing, many process parameters are still adjusted based on prior knowledge, operator experience, or trial-and-error. Such approaches offer limited quantitative insight and process transparency, which can lead to variability in cell quality, prolonged optimization cycles, and increased production waste and cost. These drawbacks highlight the importance of numerical modelling approaches capable of providing predictive understanding and systematic process optimization [9]. Through the predictive capabilities of computational modelling, the cell performance can be enhanced while reducing both R&D waste and cost. A variety of computational modeling strategies have been developed in recent years to optimize LIB manufacturing processes [10–13].

Within this context, Coarse-Grained Molecular Dynamics (CGMD), a physics-based method, offers a robust framework for explicitly modeling slurry mixing by resolving particle-level interactions between active material, carbon and binder particles. In this CGMD framework, clusters of atoms and molecules are represented as coarse-grained particles, whose interactions are governed by calibrated force-field (FF) parameters implemented in the LAMMPS software (version 29 August 2024) [14] to reproduce the thermodynamic and kinetic behavior of the system.

The recent literature demonstrates that, in CGMD-based slurry models, the active material (AM) is represented as spherical particles with a prescribed density and particle-size distribution. The carbon–binder domain (CBD) is modeled as effective spherical particles, each representing a certain mass of carbon, binder, and, in the slurry phase, solvent within a volume characterized by an effective density. Interactions between these particles are described through a combination of attractive, repulsive, frictional and dissipative forces. Specifically, van der Waals interactions are typically modeled using the Lennard-Jones (LJ) potential, whereas particle–particle contacts (frictional and dissipative forces) are described using a Granular Hertz potential (GH) [15]. These interaction potentials are governed by multiple FF parameters including the LJ energy and length scales (ε and σ) and cutoff radius (r_c) and contact stiffness, damping and friction coefficients (k_n, γ_n and X_μ) controlling particle interaction characteristics (GH potential). The selection and variation of these parameters play a key role in determining slurry behavior and the resulting macroscopic properties [16].

Despite the widespread adoption of CGMD for slurry modelling, FF parameterization remains one of the most critical and least standardized aspects of the methodology. So far, only a limited number of studies have explicitly focused on systematic parameterization strategies. Forouzan et al. [17], who developed a mesoscale particle dynamics model for simulating slurries, employed semi-empirical parameterization strategies in which LJ and GH interaction parameters were iteratively adjusted to reproduce slurry rheology and density. Subsequently, the study by Lombardo et al. [16] has explored alternative, optimization-driven parameterization frameworks, where FF parameters are identified through systematic search algorithms guided by quantitative cost functions comparing simulated and experimental slurry properties. Although their work focused on accelerating FF parameter optimization, it did not explicitly quantify and rank the individual main effects of LJ and GH parameters on simulated slurry properties. In a related study, Yao et al. [15]

conducted a sensitivity analysis of CBD particle size, CBD density, and AM particle-size sampling, rather than investigating the relative contributions of LJ and GH FF parameters. Beyond these differences in methodological focus, reported FF parameter sets vary substantially across the literature, summarized in Table 1, even among studies employing similar interaction potentials and targeting nominally comparable slurry systems. This variability is particularly pronounced when considering differences in cathode chemistries (e.g., $LiNi_{0.5}Co_{0.2}Mn_{0.3}O_2$ (NCM-523), $LiNi_{0.33}Mn_{0.33}Co_{0.33}O_2$ (NMC111), $LiNi_{0.80}Mn_{0.10}Co_{0.10}O_2$ (NMC811)), the type of conductive additives (C65 vs. C45) and solvents (N-Methyl-2-Pyrrolidone (NMP) vs. water), their formulation compositions (AM/CBD ratios), and solid content (SC) levels [15–23]. Moreover, FF parameters are often calibrated to reproduce specific target observables—such as slurry density, viscosity, or porosity—leading to system-dependent parameter choices that are not directly transferable [22].

Table 1. Summary of FF parameters reported in the literature for CGMD-based LIB cathode slurry modelling (**a**) Slurry formulations. Row identifiers link the two panels. (**b**) Lennard-Jones and Granular Hertz potential parameters for the corresponding rows in panel (**a**).

(**a**)

Row	Ref.	AM Chemistry	Carbon Additive	Solvent	Composition (AM/CBD) (%/%)	SC (%)
1	[17]	NCM523	C45	NMP	90/10	-
2	[18]	NCM523	Carbon Black	NMP	85/15, 90/10, 95/5	-
3	[16]	NMC111	C65	NMP	96/4	70, 71, 73
4	[16]	NMC111	C65	NMP	95/5	65
5	[16]	NMC111	C65	NMP	95/5	68
6	[16]	NMC111	C65	NMP	95/5	70
7	[19]	NMC111	C65	NMP	94/6	65
8	[20]	NMC111	C65	NMP	96/4	69
9	[21]	NMC811	Carbon Black	Water	90/10	70
10	[21]	NMC811	Carbon Black	NMP	90/10	70
11	[15]	NMC811	Carbon Black	NMP	97/3	74
12	[23]	NMC111, LFP, Solid State	-	-	-	-

(**b**)

Row	Ref.	ε_{AM} [pg μm^{2}μs^{-2}]	σ_{AM} [μm]	r_{c_AM} [μm]	ε_{CBD} [pg μm^{2}μs^{-2}]	σ_{CBD} [μm]	k_n [pg μm^{-1}μs^{-2}]	γ_n [μm^{-1}μs^{-1}]	X_μ [Unitless]
1	[17]	$300 \times (d_{aexp})^3$	$0.88 \times (d_{aexp})$	$1.14 \times (d_{aexp})$	10	1.1	10	18	0.001
2	[18]	$300 \times (d_{aexp})^3$	$0.88 \times (d_{aexp})$	$1.14 \times (d_{aexp})$	10	1.1	10	18	0.001
3	[16]	$0.01 \times (d_{aexp})$	$0.88 \times (d_{aexp})$	$1.14 \times (d_{aexp})$	$0.001 \times (d_{CBD})$	1.1	8	38	0.015
4	[16]	$0.01 \times (d_{aexp})$	$0.88 \times (d_{aexp})$	$1.14 \times (d_{aexp})$	$1 \times (d_{CBD})$	1.1	8	36	0.015
5	[16]	$0.01 \times (d_{aexp})$	$0.88 \times (d_{aexp})$	$1.14 \times (d_{aexp})$	$1 \times (d_{CBD})$	1.1	8	38	0.015
6	[16]	$0.01 \times (d_{aexp})$	$0.95 \times (d_{aexp})$	$1.14 \times (d_{aexp})$	$1 \times (d_{CBD})$	1.1	8	38	0.015
7	[19]	$0.01 \times (d_{aexp})$	$0.95 \times (d_{aexp})$	$1.14 \times (d_{aexp})$	$1 \times (d_{CBD})$	1.1	7	45	0.015
8	[20]	$0.01 \times (d_{aexp})$	$0.88 \times (d_{aexp})$	$1.14 \times (d_{aexp})$	$0.001 \times (d_{CBD})$	1.1	8	30	0.015
9	[21]	$0.01 \times d$	$0.88 \times d$	$1.14 \times d$	$0.0005 \times d$	1.1	2	12	0.001
10	[21]	$0.01 \times d$	$0.88 \times d$	$1.14 \times d$	$0.001 \times d$	1.1	10	18	0.001
11	[15]	$0.01 \times d$	$0.88 \times d$	$1.14 \times d$	$0.001 \times d$	1.1	10	18	0.001
12	[23]	0.834–1.263	0.634–1.029	1.285–1.734	0.842–1.202	0.924–0.930	1.697–5.460	25.028–36.216	0.013–0.017

Despite the availability of reported FF parameter sets for CGMD slurry modelling, the relative contributions of the underlying LJ and GH FF parameters to slurry density have not been systematically quantified. To address this gap, literature-derived LJ and GH FF parameter ranges are systematically evaluated through a DOE-based sensitivity analysis. The proposed methodology quantitatively identifies the dominant parameters governing

slurry density and provides a rational basis for FF parameter selection. Subsequently, the FF parameter set selected through density-based optimization is assessed using non-equilibrium molecular dynamics (NEMD) viscosity simulations together with experimental rheological measurements, thereby evaluating the applicability of the selected parameters to an independent rheological response beyond the optimization target. This approach provides a systematic methodology for both identifying the governing FF parameters and assessing the broader applicability of the selected parameter set in CGMD slurry simulations.

2. Materials and Methods

2.1. Slurry Composition and Material Properties

In this study, a single NMC111-based cathode slurry formulation was examined to evaluate the applicability and performance of FF parameter ranges reported in the literature [23]. This cathode slurry consists of 85 wt% AM (NMC111), 9 wt% conductive additives (Super C65 carbon black), and 6 wt% polyvinylidene fluoride (PVDF), on a dry-solid basis. The solid content (SC), defined as the mass fraction of solid components relative to the total slurry mass, was set to 46 wt%. The composition was selected based on the availability of experimental slurry density data reported in the literature [22], which enabled a direct and quantitative analysis of the simulation results. In the slurry model, CBD particles represent the carbon–binder components together with implicitly included NMP, using an effective CBD diameter of 7 μm and density of 0.05 g cm^{-3}. The diameter is consistent with the liquid-state CBD diameter reported in [23] for an NMC111 slurry phase. The particle-number calculation and the relationship between the solvent-free and slurry CBD representations are described in Section 2.2.1. Furthermore, the AM was modeled using discrete particle sizes of 2.5, 3.5, 4.5, 5.86, 8.28, and 10.35 μm based on experimental scanning electron microscopy (SEM) measurements reported in [20], with its intrinsic density set to 4.65 g cm^{-3}. The specific classification of these material phases by their representative diameters and their resulting spatial distribution within the simulation domain are illustrated in Figure 1.

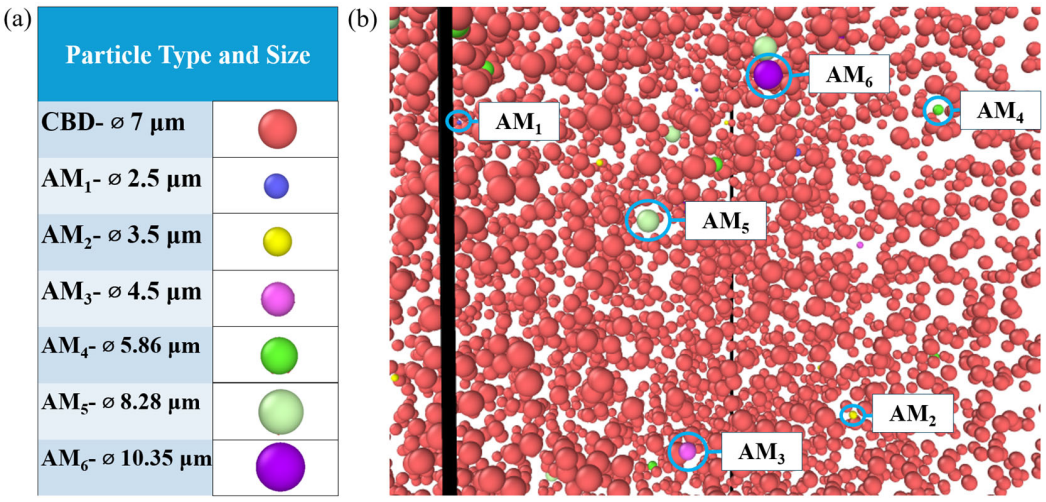


Figure 1. Representation of the multicomponent slurry system: (**a**) classification table of carbon–binder domain (CBD) and Active Material (AM) particles by their respective diameter (⌀) classes; (**b**) visualization of the spatial distribution of AM and CBD particles within the simulation cell, where different colors indicate specific size classes (AM_1 to AM_6).

To provide reference data for density and rheological characterization, the modelled NMC111 cathode slurry composition was also prepared experimentally. $LiNi_{1}/_{3}Mn_{1}/_{3}Co_{1}/_{3}O_{2}$ (NMC111, $\rho = 4.65$ g cm^{-3}) was used as the AM. Super C65 carbon black and PVDF were supplied by MTI Corporation (Richmond, CA, USA), and N-methyl-2-pyrrolidone (NMP, $\rho = 1.03$ g cm^{-3}) was purchased from Acros Organics (Geel, Belgium). The solid components (NMC111, carbon black, and PVDF) were first dry-mixed. Subsequently, NMP was added until the target solid content of 46 wt% was reached. The slurry was then mixed in an Optosense high-shear mixer (Optosense, Winter Park, FL, USA) at 165 rpm for 2 h at 25 ± 1 °C.

The slurry density was measured using an Anton Paar Ultrapyc 5000 gas pycnometer (Anton Paar GmbH, Graz, Austria). The sample was weighed, and its mass was entered into the instrument. Density was calculated from the entered mass and the sample volume determined by gas displacement. Measurements were performed using the reference-first flow direction to reduce the influence of solvent vapor pressure, a feature particularly useful for slurries containing solvents with high vapor pressures. Measurement cycles were repeated until the selected repeatability criterion of better than 0.1% was achieved.

Rheological measurements were performed using a Lamy Rheology CP4000 Plus rotational rheometer (LAMY Rheology, Champagne-au-Mont-d'Or, France) at room temperature (25 ± 1 °C). Viscosity measurements were conducted at constant shear rates of 65, 173, and 500 s^{-1}, together with a shear-rate ramp test from 65 to 500 s^{-1}, with data collected for 300 s in each test.

2.2. Model Workflow

2.2.1. Particle Generation

A reference dry-electrode mass of 0.100 µg was used to determine the particle population. This mass was partitioned into AM and solvent-free CBD according to their dry-solid mass fractions of 85 wt% and 15 wt%, respectively. The volume of each phase was calculated by dividing its mass by the corresponding density: 4.65 g cm^{-3} for NMC111 (AM) and 0.9 g cm^{-3} for solvent-free CBD. The solvent-free CBD density of 0.9 g cm^{-3} and particle diameter of 1.3 µm were adopted from the NMC111 parameters reported in [23].

The number of particles was determined by assigning a representative diameter of 1.3 µm for solvent-free CBD and six AM particle-size classes (2.5, 3.5, 4.5, 5.86, 8.28, 10.35 µm) obtained from the literature [20]. The AM volume assigned to each diameter class was calculated using histogram-derived class coefficients from [20]. Each class volume was divided by the corresponding spherical particle volume. Similarly, the CBD population was calculated by dividing the total solvent-free CBD volume by the volume of a single 1.3 µm spherical particle. The resulting system consisted of 138 AM particles and 14,488 CBD particles.

For the slurry representation, the solvent mass required to achieve a solid content of 46 wt% was calculated from the reference dry-solid mass and added to the total solvent-free CBD mass. The combined mass was then divided by the effective density of 0.05 g cm^{-3} to obtain the total effective CBD volume. This volume was divided by the previously determined number of CBD particles, 14,488, to obtain the volume of a single particle. The effective particle diameter was subsequently calculated from this volume using the spherical geometry of the CBD particles, yielding 7 µm, consistent with the liquid-state CBD diameter reported in [23]. The initial packing of the multicomponent slurry system within the simulation domain and the corresponding quantitative distribution of each particle class are visualized in Figure 2.

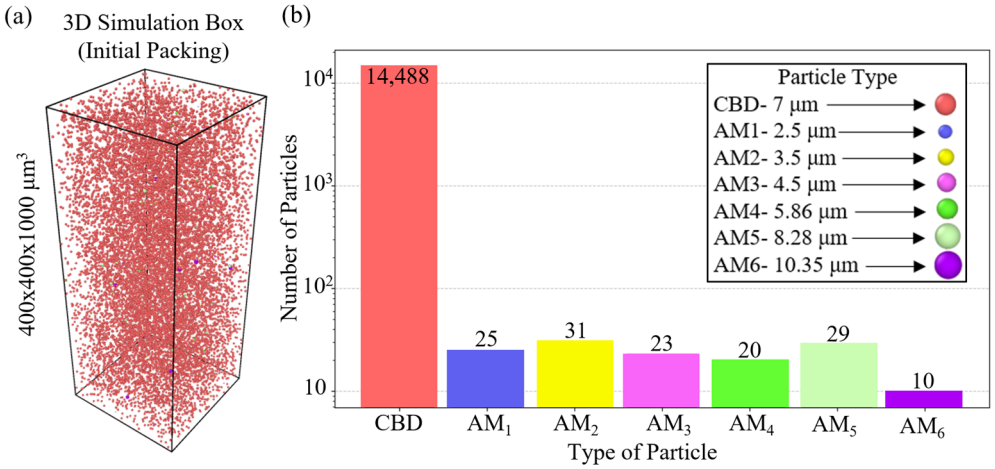


Figure 2. Initial system configuration: (**a**) 3D simulation box representing the packing of 138 AM particles and 14,488 effective CBD particles; (**b**) particle counts for the six AM diameter classes and the CBD particles. The effective CBD particle diameter in the slurry model is 7 µm.

The particle configuration generated in this step was first used as the initial input for the density equilibration simulation. After applying the optimized LJ and GH FF parameters, the system was equilibrated until the slurry density reached a converged state. The final equilibrated particle coordinates were then exported and used as the initial configuration for the subsequent viscosity simulation. In this way, the viscosity calculation was not started from a randomly generated structure, but from the converged slurry morphology obtained after density equilibration.

2.2.2. Coarse-Grained Molecular Dynamics

This study employed a CGMD approach using LAMMPS to investigate the influence of selected material and interaction parameters on the density of an NMC111-based cathode slurry, and to calculate the apparent shear viscosity of the optimized slurry configuration. The density equilibration simulations were carried out at constant particle number, pressure and temperature (NPT), specifically at 300 K and 1 atm, to represent the equilibrium state of the slurry. The model contained two particle populations: AM particles representing NMC111 and effective CBD particles representing carbon, binder, and solvent. The solvent was not modeled as a separate particle population. The interparticle interactions were controlled by a combination of two force fields: Shifted-Force Lennard-Jones (LJ/SF) potential, which accounts for van der Waals-type interactions (adhesion forces), and the GH model, which captures elastic contact, frictional and dissipative forces between particles. The combination of these two models enabled the simulation of attractive and repulsive interactions, as well as damping effects, which are essential for the representation of slurry microstructural dynamics.

The mathematical expression for the LJ potential is defined as follows:

$$E_{LJ}(r) = 4\varepsilon\left[\left(\frac{\sigma}{r}\right)^{12} - \left(\frac{\sigma}{r}\right)^{6}\right] \quad (1)$$

The interparticle force is obtained by taking the negative gradient of the LJ potential energy function as expressed in Equation (2), which describes the balance of attractive and repulsive interactions as a function of interparticle distance.

$$F_{LJ}(r) = -\nabla E_{LJ}(r) \quad (2)$$

In this framework, σ defines the distance where the potential is zero, while ε determines the strength of the attractive force between particles. The LJ potential and its characteristic parameters, ε and σ, are illustrated in Figure 3, demonstrating the relationship between interparticle distance and potential energy. A higher ε value indicates stronger attraction, whereas a lower ε corresponds to weaker attraction or stronger repulsion.

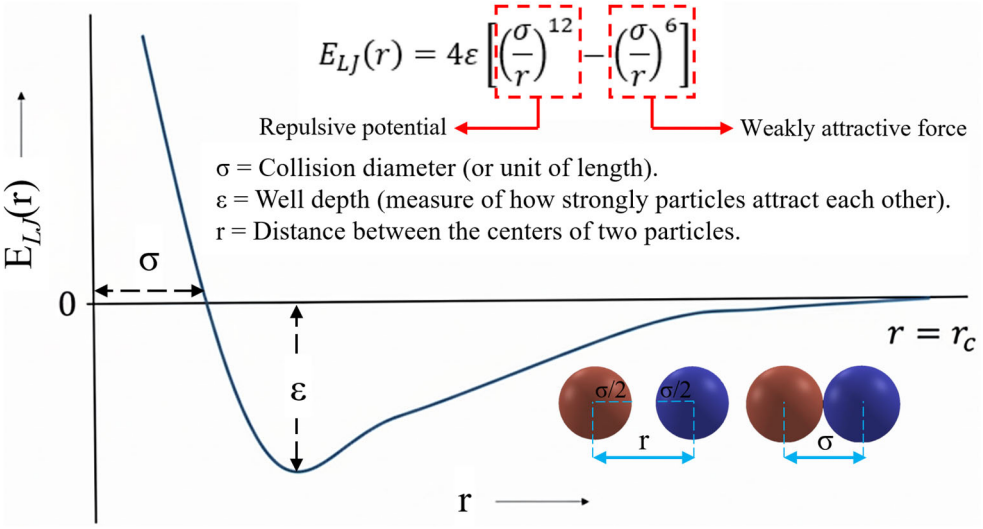


Figure 3. LJ potential profile showing the relationship between interparticle distance (r) and energy (E_{LJ}), with key parameters σ (collision diameter), ε (well depth), and r_c (cutoff distance) indicated.

The LJ/SF potential adds a linear correction to the standard LJ potential to eliminate interactions beyond the cutoff distance r_c, ensuring a smooth decay of both potential and force at that point. As defined in Equation (3), the LJ/SF force subtracts the force contribution evaluated at the cutoff distance, thereby guaranteeing that both the potential and force decay continuously to zero at r_c. For particle separations greater than or equal to the cutoff distance, the interaction force is explicitly set to zero, as shown in Equation (4), eliminating unphysical discontinuities in the FF.

$$F_{LJ/SF}(r) = F_{LJ}(r) - F_{LJ}(r_c)\ r < r_c \tag{3}$$

$$F_{LJ/SF}(r) = 0\ r \geq r_c \tag{4}$$

The slurry exhibits a suspension-like structure, and due to the presence of binder, adhesive forces and effective bonding behavior occur between the particles. To model these interactions, the LJ/SF potential is employed, which depends on three fundamental parameters: ε, σ and r_c.

On the other hand, the GH model describes elastic, dissipative and frictional forces between granular particles during contact. The GH contact force is expressed as follows:

$$F_{GH} = \sqrt{\delta}\sqrt{\frac{R_i R_j}{R_i + R_j}}\left[\left(k_n \delta \mathbf{n}_{ij} - m_{eff}\gamma_n \mathbf{v}_n\right) - \left(k_t \Delta s_t + m_{eff}\gamma_t \mathbf{v}_t\right)\right] \tag{5}$$

The GH contact force includes both normal and tangential components, defined by elastic constants k_n and k_t, damping coefficients γ_n and γ_t, and relative velocity components $\mathbf{v}_n$ and $\mathbf{v}_t$, respectively. The force also depends on the tangential displacement vector Δs_t, and effective mass m_{eff} and the unit vector connecting the centers of two interacting particles $\mathbf{n}_{ij}$. The variables R_i and R_j represent the particle radii, while δ represents the overlap distance. The final parameter considered is the friction coefficient X_μ, defined as the maximum allowable ratio of tangential to normal forces.

Particle overlap was quantified as $\delta_{ij} = max[0, R_i + R_j - r_{ij}]$, where r_{ij} is the periodic minimum-image distance between particle centers and R_i and R_j are the contact radii assigned in the simulation. The normalized overlap was defined as $\delta_{ij} / min(R_i, R_j)$. Distributions were evaluated separately for CBD–CBD, AM–CBD, and AM–AM contacts, counting each contacting pair once per snapshot and excluding non-contacting pairs. The analysis used the assigned simulation contact radii, including the factor of 1.14 applied to the experimental AM diameters.

For the viscosity calculation, the final equilibrated slurry morphology obtained from the density equilibration simulation was used as the starting configuration. A non-equilibrium molecular dynamics (NEMD) approach was then applied by imposing a simple shear deformation on the simulation box. The shear flow was generated using an SLLOD-based formulation together with a deforming simulation cell, while the temperature was controlled using a deformation-aware thermostat. Constant shear rates of 65 s^{-1} and 500 s^{-1} were applied, and the off-diagonal P_{xy} component of the pressure tensor was monitored throughout each simulation. The macroscopic shear stress was defined according to the LAMMPS sign convention as ($\tau_{xy} = -P_{xy}$) and the apparent shear viscosity was calculated from the ratio of the time-averaged shear stress to the imposed shear rate, as given in Equation (6).

$$\eta = \frac{\tau_{xy}}{\dot{\gamma}} = -\frac{P_{xy}}{\dot{\gamma}} \tag{6}$$

where η is the apparent shear viscosity, P_{xy} is the off-diagonal (xy) component of the pressure tensor obtained from LAMMPS, ($\tau_{xy} = -P_{xy}$) is the corresponding macroscopic shear stress, $\dot{\gamma}$ is the applied shear rate, and the angle brackets denote time averaging over the viscosity-evaluation interval.

2.2.3. Simulation Conditions

For the density equilibration simulation, all particles were initially placed randomly in a large simulation box measuring 400 × 400 × 1000 μm^3 to minimize excessive initial overlap and were assigned random velocities corresponding to a temperature of 300 K. Particle overlap was subsequently allowed to represent the deformable and wet nature of the slurry structure. The density equilibration simulation was performed for 15 × 10^6 timesteps with a timestep of $\Delta t = 0.0001$ μs. The slurry density was monitored during the simulation and the final equilibrated configuration was used for the subsequent viscosity calculation.

Periodic boundary conditions were applied in all three spatial directions (x, y, and z), such that particles crossing a simulation boundary re-entered through the corresponding opposite boundary. The integration timestep determines the temporal resolution of particle motion and may affect the accuracy of instantaneously calculated quantities. A relative deviation below 1% was adopted as the acceptance criterion.

For the viscosity simulation, the equilibrated slurry configuration obtained from the density equilibration step was used as the initial structure. Prior to applying shear, the system was further relaxed under zero-shear conditions for 10 × 10^6 timesteps to obtain a stable initial state. Separate NEMD simulations were performed at constant shear rates of 65 and 500 s^{-1}, and the corresponding off-diagonal P_{xy} component of the pressure tensor was monitored throughout each simulation. Each production simulation was continued for an additional 20 × 10^6 timesteps using a timestep of $\Delta t = 0.0005$ μs.

A fixed random seed was used to maintain consistent initial conditions across the simulations. Repeated runs using identical settings and the same seed yielded identical results; consequently, such repetitions were not used to estimate statistical uncertainty or construct error bars. Different-seed simulations have been reported in [22]; however, a

systematic multi-seed uncertainty assessment was not performed for the present parameter sets, which limits conclusions regarding run-to-run variability.

The simulations were performed on the ARF system at TÜBİTAK using a single computing node equipped with 256 GB RAM and an Intel(R) Xeon(R) Platinum 8480+ processor operating at 2.0 GHz with 112 cores.

2.3. Design of Experiments

A DOE approach was employed to systematically investigate the influence of the selected FF parameters on the slurry density simulated by the CGMD model. In this context, eight formulation-related parameters—comprising the LJ terms (ε_{AM}, σ_{AM}, r_{c_AM}, ε_{CBD}, σ_{CBD}) and the GH terms (k_n, γ_n, X_μ)—were treated as independent factors. The values of the LJ and GH FF parameters used in the CGMD modelling performed in LAMMPS are listed in Table 2.

Table 2. Literature-based mean values and bounds of the selected FF parameters for NMC111. Adapted from Ref. [23], licensed under CC BY.

Factors	Units	Mean Values	Lower Bound	Upper Bound
ε_{AM}	pg μm^{2}μs^{-2}	1	0.834	1.263
σ_{AM}	μm	0.879	0.634	1.029
r_{c_AM}	μm	1.47	1.285	1.734
ε_{CBD}	*pg* μm^{2}μs^{-2}	1	0.842	1.202
σ_{CBD}	μm	0.989	0.924	0.930
k_n	*pg* μm^{-1}μs^{-2}	3.31	1.697	5.460
γ_n	μm^{-1}μs^{-1}	29.70	25.028	36.216
X_u	Unitless	0.014	0.013	0.017

The CBD LJ length-scale parameter (σ_{CBD}) values in Table 2 are reproduced as reported in [23]. The reported mean (0.989 μm) is outside the listed lower and upper bounds (0.924–0.930 μm); the values are retained here for consistency with the cited source. The two-level DOE design uses the stated lower and upper bounds for this factor.

A full factorial design with eight two-level factors would require $2^8 = 256$ independent CGMD simulations. Since each simulation involves long equilibration times and substantial computational cost, performing a full factorial design was not practical for the present screening study. Therefore, to efficiently explore this multidimensional parameter space while maintaining a manageable computational cost, a $2^{(8-4)}$ fractional factorial design with Resolution IV was adopted, following the approach applied by Meibodi et al. [24] for an eight-factor system. This design reduced the required number of simulations to 16 while still allowing the dominant parameter effects to be identified. The resulting 16-run design enabled the evaluation of the main effects of the selected FF parameters on slurry density.

A Resolution IV design was specifically chosen because, in this design structure, main effects are not aliased with each other or with two-factor interactions. This enables the primary influence of each FF parameter on slurry density to be evaluated independently. The objective of this stage was to perform a screening analysis to identify the dominant FF parameters controlling the simulated slurry density, rather than to exhaustively resolve interaction effects.

Accordingly, LAMMPS simulations were performed for each DOE case, corresponding to different combinations of upper and lower bound values of the selected FF parameters. The resulting slurry density values were then analyzed using main-effects plots and Pareto charts. This systematic investigation allowed a clear interpretation of the model behavior, highlighting which parameters exert the strongest control over the slurry density.

Slurry density was selected as the primary calibration target to constrain the macroscopic mass-to-volume relationship for the specified formulation. It was used as a composition-based constraint on the represented slurry volume, rather than as an independently emergent property. The sensitivity of the simulated density to the interaction parameters therefore characterizes the effective packing and overlap response of the coarse-grained model under the applied simulation protocol. Viscosity was excluded from the calibration objective and reserved for a subsequent assessment of rheological transferability.

In addition to the DOE-based sensitivity analysis, a desirability-based response optimization procedure was performed to identify the FF parameter combination that best reproduces the experimentally measured slurry density. The simulated slurry density was defined as the response variable, and the optimization objective was set as a target response rather than a maximization or minimization problem. The target density was taken as 1.55 g cm^{-3} based on the experimental value reported in the literature [22]. The optimization was carried out by maximizing the composite desirability function, where a desirability value close to 1 indicates that the predicted response is close to the target value.

3. Results and Discussion

3.1. Assessment of Literature-Based FF Parameters

To establish a reference point for the subsequent sensitivity analysis, CGMD simulations were first performed using three FF parameter sets comprising, respectively, the lower-bound, mean, and upper-bound values reported by Vijay et al. [23] for NMC111 and summarized in Table 2. Since these parameter ranges were originally developed for an NMC111 slurry with an effective CBD particle diameter of 7 μm, the same CBD diameter was adopted in the present study to ensure consistency with the original parameterization framework. The investigated slurry had a dry-solid composition of 85 wt% AM and 15 wt% CBD, and a solid content of 46 wt%. Solvent was represented within the effective CBD particles, as described in Section 2.1.

Using the literature-based mean parameter values, the predicted slurry density was 1.366 g cm^{-3}, corresponding to an approximately 11.9% deviation from the experimentally reported density of 1.55 g cm^{-3} [22]. Simulations were then repeated using the lower- and upper-bound parameter sets. The lower-bound combination produced a density of 1.931 g cm^{-3} (24.6% deviation), whereas the upper-bound combination resulted in a density of 1.064 g cm^{-3} (31.4% deviation). The corresponding results are summarized in Table 3.

Table 3. The performance of literature-based FF parameter sets for simulated slurry density.

FF Parameter Sets	Simulated Density (g cm^{-3})	Experimental Density (g cm^{-3}) [22]	Deviations (%)
Lower-bound values	1.931	1.55 ± 0.05	24.6
Mean values	1.366	1.55 ± 0.05	11.9
Upper-bound values	1.064	1.55 ± 0.05	31.4

These results demonstrate that the three literature-based FF parameter sets evaluated produce substantial variation in simulated slurry density and do not directly reproduce the experimental density for the investigated slurry composition. Therefore, a systematic DOE-based sensitivity analysis was performed to identify the dominant FF parameters governing slurry density.

3.2. DOE-Based Screening of FF Parameters

To systematically screen the influence of individual LJ and GH FF parameters on slurry density, a two-level fractional factorial DOE approach was adopted. All FF parameters (ε_{AM}, σ_{AM}, r_{c_AM}, ε_{CBD}, σ_{CBD}, k_n, γ_n and X_μ) were varied at two levels corresponding to

the lower and upper bounds reported in Table 2 (Section 2.3). Within this framework, the selected FF parameters were varied within their specified ranges, and the corresponding parameter combinations and their simulated slurry density outputs are listed in Table 4. The simulated slurry density ranged from 1.06386 to 1.9305 g cm^{-3}, the influence of the selected FF parameters on this variation is discussed in detail in the following section.

Table 4. Performance of literature-based FF parameter sets in predicting slurry density.

Run	ε_{AM}	σ_{AM}	r_c _AM	ε_{CBD}	σ_{CBD}	k_n	γ_n	X_μ	Simulated Slurry Density (g cm^{-3})
1	0.834	1.029	1.285	0.842	0.930	1.697	36.216	0.017	1.86939
2	1.263	1.029	1.285	0.842	0.930	5.460	25.028	0.013	1.06399
3	0.834	1.029	1.285	1.202	0.924	5.460	36.216	0.013	1.06419
4	0.834	0.634	1.285	1.202	0.930	5.460	25.028	0.017	1.07915
5	1.263	0.634	1.285	0.842	0.924	5.460	36.216	0.017	1.07907
6	0.834	0.634	1.734	1.202	0.924	1.697	36.216	0.017	1.93211
7	1.263	1.029	1.734	1.202	0.930	5.460	36.216	0.017	***1.06386***
8	1.263	0.634	1.285	1.202	0.930	1.697	36.216	0.013	1.93143
9	1.263	0.634	1.734	1.202	0.924	5.460	25.028	0.013	1.07914
10	1.263	1.029	1.734	0.842	0.924	1.697	36.216	0.013	1.87066
11	0.834	0.634	1.734	0.842	0.930	5.460	36.216	0.013	1.07913
12	0.834	1.029	1.734	1.202	0.930	1.697	25.028	0.013	1.87375
13	1.263	0.634	1.734	0.842	0.930	1.697	25.028	0.017	1.93071
14	0.834	1.029	1.734	0.842	0.924	5.460	25.028	0.017	1.06564
15	1.263	1.029	1.285	1.202	0.924	1.697	25.028	0.017	1.86485
16	0.834	0.634	1.285	0.842	0.924	1.697	25.028	0.013	***1.93050***

3.3. Screening of Factors That Affect Slurry Density

To identify the dominant LJ and GH FF parameters governing slurry density, the results of the two-level fractional factorial DOE were evaluated using Pareto screening, normal probability analysis, and analysis of variance (ANOVA). The Pareto chart presents the absolute magnitudes of the effects and includes a reference line, enabling the rapid identification of effects that exceed the reference line and may therefore be considered potentially important. The chart provides the relative importance of the FF parameters, as shown in Figure 4.

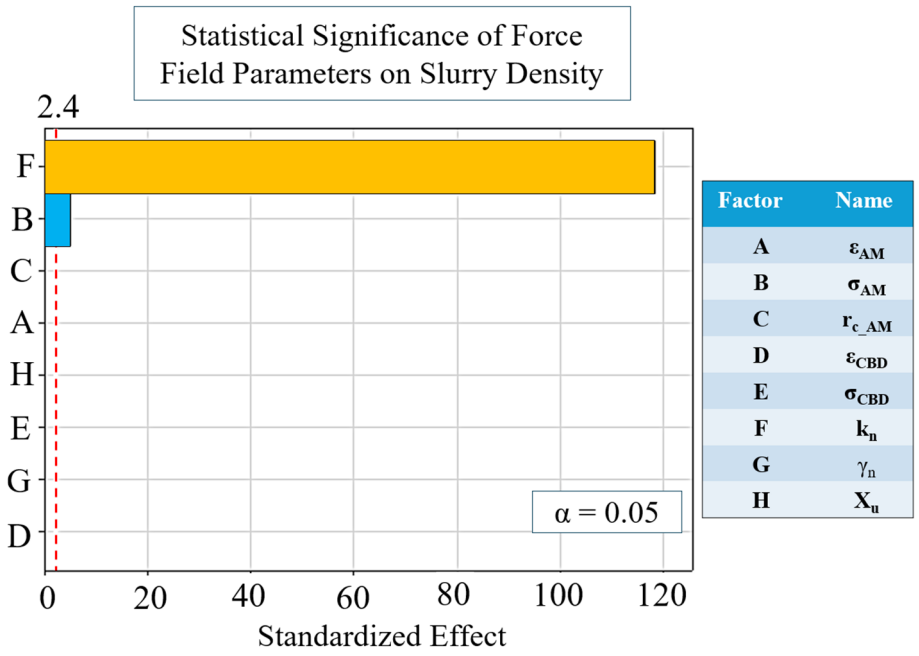


Figure 4. Pareto chart of the standardized effects of FF parameters on slurry density. The red dashed vertical line indicates the critical threshold for statistical significance at $\alpha = 0.05$.

The analysis shows that factor F(k_n) exhibits the largest standardized effect by a substantial margin, indicating that slurry density is predominantly controlled by the normal contact elastic constant in the GH normal contact formulation. The second most influential parameter is the LJ distance parameter of the AM, B (σ_{AM}), highlighting the role of the effective interaction distance of AM particles in determining slurry density. Nevertheless, its effect remains considerably smaller than that of k_n, demonstrating the dominant contribution of normal contact stiffness.

To quantify the statistical significance of the effects of selected LJ and GH FF parameters (ε_{AM}, σ_{AM}, r_{c_AM}, ε_{CBD}, σ_{CBD}, k_n, γ_n, and X_μ) on simulated slurry density and to identify which main effects govern the variation in slurry density, an ANOVA was performed. Prior to the ANOVA, a Box–Cox transformation with $\lambda = 0.5$ was applied to the simulated slurry density response. The ANOVA results presented in Table 5 were obtained using the transformed response. The statistical significance of each effect was estimated using the associated p-values, with effects exhibiting p-values below 0.05 considered statistically significant at a 95% confidence level. The results demonstrate that the developed DOE model is statistically significant, since the p-value was less than 0.05. That is, the selected parameters collectively have a strong influence on slurry density. The corresponding ANOVA results are reported in Table 5.

Table 5. Analysis of variance for the square-root-transformed slurry density response.

Source	Degrees of Freedom	Sequential Sum of Squares	Contribution (%)	F-Value	*p*-Value
Model	8	0.472167	99.95	1760.96	<0.001
Linear			99.95	1760.96	<0.001
ε_{AM}	1	<0.001	<0.001	0.03	0.869
σ_{AM}	1	0.000865	0.18	25.82	0.0018
r_{c_AM}	1	<0.001	<0.001	0.04	0.845
ε_{CBD}	1	<0.001	<0.001	0.00	0.986
σ_{CBD}	1	<0.001	<0.001	0.01	0.944
k_n	1	0.471298	99.77	14,061.79	<0.001
γ_n	1	<0.001	<0.001	0.00	0.981
X_μ	1	<0.001	<0.001	0.01	0.908
Residual	7	0.000235	0.05	-	-
Total	15	0.472401	100.00	-	-

Among the investigated FF parameters, the normal contact elastic constant (k_n) was identified as the dominant factor governing slurry density. With a contribution of 99.77%, an F-value of 14,061.79, and a p-value below 0.001, k_n overwhelmingly controls the variation in the simulated slurry density within the investigated parameter space. In comparison, the LJ distance parameter of the AM (σ_{AM}) also exhibited a statistically significant effect ($p = 0.001$); however, its contribution was only 0.18%, indicating a much smaller influence than that of k_n. The remaining parameters, including ε_{AM}, r_{c_AM}, ε_{CBD}, σ_{CBD}, γ_n, and X_μ, showed negligible contributions and did not exhibit statistically significant effects ($p > 0.05$) within the investigated ranges. For σ_{CBD}, the particularly narrow investigated range (0.924–0.930 µm), adopted directly from [23], may contribute to the negligible effect observed on slurry density. Overall, the ANOVA results confirm that the variability in slurry density is governed predominantly by the normal contact stiffness, while the influence of the remaining FF parameters is comparatively limited.

To further interpret the direction of these effects, the standardized effects are examined using the normal probability plot shown in Figure 5a. The plot can be divided into two distinct regions separated by the 50% line. Effects located below this line correspond to negative coefficients, indicating that an increase in the corresponding parameter level leads to a decrease in slurry density, whereas effects located above the line represent

positive coefficients, implying an increase in density with increasing parameter level. The statistical significance of each effect is assessed based on its deviation from the reference line passing through the zero standardized effect. Points lying close to this line, shown as circles, are considered statistically insignificant and are associated with the estimated numerical uncertainty of the model, while effects represented by squares and located further away from the reference line are regarded as statistically significant within investigated parameter ranges.

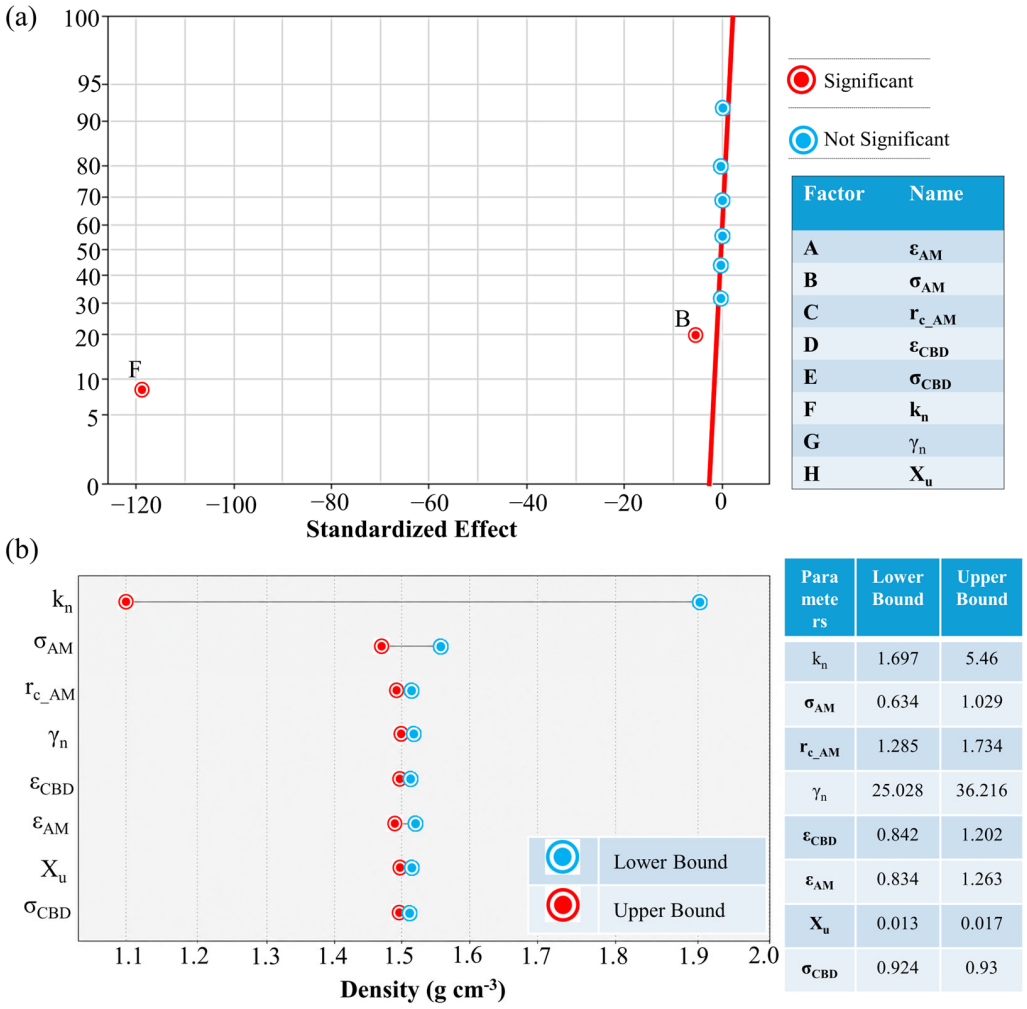


Figure 5. (**a**) Normal probability plot of standardized effects of FF parameters on slurry density and (**b**) main effect plot for slurry density.

As observed in Figure 5a, factor F(k_n) is the most influential parameter contributing to a reduction in slurry density. The large negative effect indicates that increasing the elastic constant for normal contact force leads to a pronounced decrease in the simulated slurry density. This trend is further supported by the main effects plot presented in Figure 5b. As the elastic constant increases from $k_n = 1.697$ to $k_n = 5.460$, the simulated slurry density decreases markedly, dropping from approximately 1.90 g cm^{-3} to nearly 1.07 g cm^{-3}.

This trend is consistent with the nature of the GH contact model, which describes repulsive interactions between neighboring particles when they overlap. That is, it highlights the dominant role of mechanical contact interactions in governing particle packing and compressibility within the slurry.

Notably, the elastic constant k_n is defined in terms of the shear modulus G and the Poisson's ratio v, with $k_n = \frac{4G}{3(1-v)}$ while the shear modulus itself is linked to Young's modulus (E) through $G = \frac{E}{2(1+v)}$ [14]. This relationship highlights that increasing k_n corresponds to mechanically stiffer particle contacts and greater resistance to deformation during collisions (Figure 6).

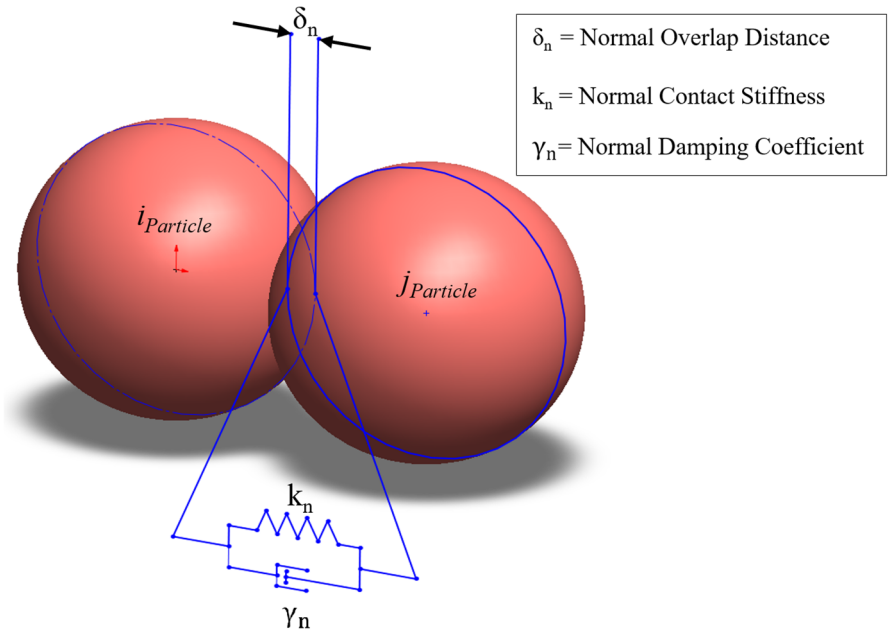


Figure 6. Schematic illustration of two particles in contact with a normal overlap distance δ. The red spheres represent the interacting particles, while the blue lines illustrate the contact geometry and associated mechanical model.

Within this context of the GH potential's normal force formulation, the normal contact force is governed by a contact force $k_n \delta \mathbf{n}_{ij}$ [25], where δ represents the particle overlap and $\mathbf{n}_{ij}$ is the unit vector connecting the particle centers. Consequently, larger values of k_n increase the magnitude of the elastic repulsive normal force for a given overlap, leading to mechanically stiffer contacts and reduced particle deformation. This interpretation is consistent with the equilibrium packing structure shown in Figure 7. Run 16 ($k_n = 1.697$) reached a compact equilibrium configuration with simulation-box dimensions of $L_x = L_y = 35.65$ µm and $L_z = 89.12$ µm, corresponding to a slurry density of 1.9305 g cm^{-3}. In contrast, Run 7 ($k_n = 5.460$) equilibrated to a substantially larger simulation box ($L_x = L_y = 43.48$ µm and $L_z = 108.69$ µm), resulting in a lower slurry density of 1.06386 g cm^{-3}. These observations are consistent with the expected influence of contact stiffness on effective packing within the adopted coarse-grained model.

Following the dominant effect of the normal contact elastic constant (k_n), the second most influential factor contributing to slurry density reduction is the AM LJ distance parameter, B (σ_{AM}), as shown in Figure 5a. Unlike k_n, which primarily governs particle compressibility through the GH contact model, σ_{AM} in the LJ potential defines the characteristic interaction distance between AM particles and therefore influences their equilibrium separation. As σ_{AM} increases, particles tend to equilibrate at larger separation distances, reducing their ability to approach one another closely. Consequently, a larger σ_{AM} enhances excluded-volume effects, preventing AM particles from approaching each other as closely. This reduction in packing efficiency leads to a lower simulated slurry density. This behavior is also evident from the main-effects plot presented in Figure 5b. Increasing σ_{AM} from 0.634 to 1.029 µm decreases the predicted slurry density from approximately 1.47 to 1.43 g cm^{-3}.

Although this reduction is considerably smaller than that produced by variations in k_n, these results further indicate that the effective interaction distance governed by σ_{AM} represents the second most influential parameter controlling the simulated slurry density within the investigated FF parameter space.

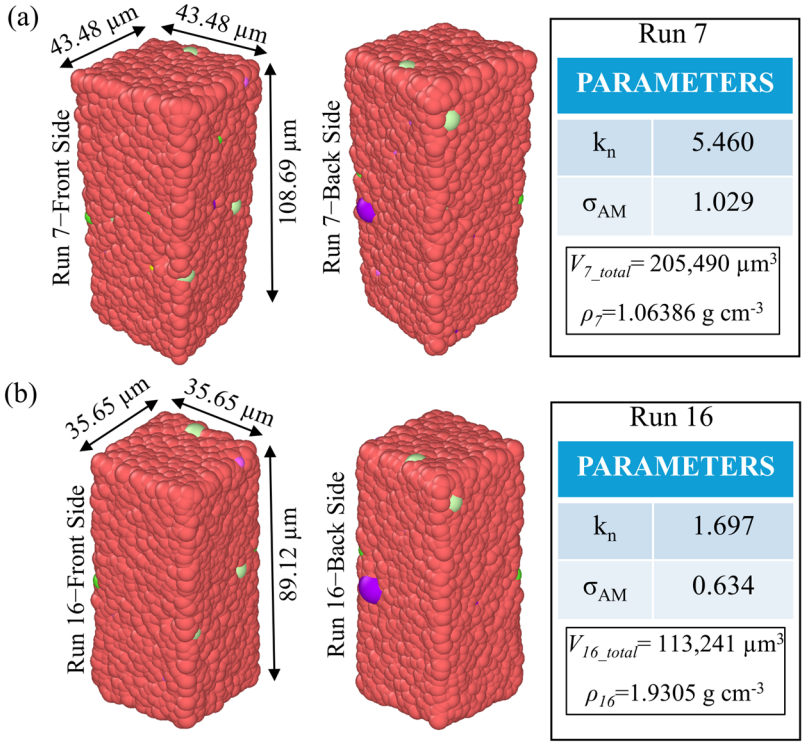


Figure 7. Equilibrium slurry morphologies obtained for (**a**) Run 7 and (**b**) Run 16 after density equilibration. The corresponding simulation-box dimensions, equilibrium volume, slurry density, the corresponding FF parameters (k_n and σ_{AM}) are shown for comparison. The particle colors correspond to the particle types defined in Figure 2.

3.4. Verification of the DOE-Based Sensitivity Analysis

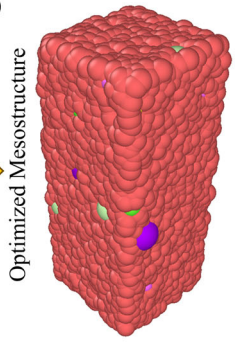
Following the identification of the dominant FF parameters, a desirability-based response optimization was performed to determine the parameter combination that most closely reproduces the experimentally reported slurry density. The optimization objective was to achieve a target slurry density of 1.55 g cm^{-3}, with lower and upper acceptable limits of 1.50 and 1.60 g cm^{-3}, respectively. All FF parameters were allowed to vary continuously within the lower and upper bounds defined in Table 2.

A desirability-based response optimizer was subsequently employed to identify the FF parameter combination that most closely satisfied the target slurry density. The resulting optimized FF parameters, together with the DOE model's predicted density of 1.550 g cm^{-3} and a composite desirability of 0.99999, are presented in Figure 8a. A new CGMD simulation was then performed using this optimized parameter set under the same particle composition, particle-size distribution, thermodynamic conditions, and equilibration procedure employed in the DOE simulations. The final equilibrated mesostructure obtained from this confirmation run is shown in Figure 8b. As summarized in Figure 8c, the CGMD simulation yielded an equilibrated slurry density of 1.407 g cm^{-3}, corresponding to a deviation of approximately 9.23% from the experimental target of 1.550 g cm^{-3}.

(a)

Optimized Parameters	
ε_{AM}	1.07233
σ_{AM}	0.977131
r_{c_AM}	1.50963
ε_{CBD}	1.02745
σ_{CBD}	0.927001
k_n	3.09873
γ_n	25.028
X_u	0.017
Predicted density (g cm^{-3})	1.55
Composite desirability	0.99

(b)



(c)

Parameter	Value
Experimental Density	1.550
Density Obtained from the Confirmation CGMD Simulation	*1.407*
Deviation from Experiment	*9.23%*

Figure 8. Density confirmation workflow following response optimization: (**a**) optimized FF parameters obtained from the response optimization, (**b**) equilibrated slurry mesostructure obtained from the confirmation CGMD simulation using the optimized parameter set, and (**c**) comparison of the predicted, simulated, and experimental slurry densities.

The discrepancy between the response-surface prediction (1.550 g cm^{-3}) and the CGMD confirmation result (1.407 g cm^{-3}) may arise from the limited ability of the 16-run fractional factorial DOE to capture nonlinear effects and parameter interactions, as the design primarily focuses on main-effect screening. Unlike the literature-based mean parameter set, which was used solely as a reference, the proposed FF parameter set was systematically selected for the investigated slurry composition, yielding a 9.23% density deviation in the confirmation simulation. Therefore, the main contribution of this study lies in the systematic identification and selection of influential FF parameters rather than achieving an exact match with the experimental density.

Figure 9 compares the slurry densities obtained from CGMD simulations performed using the lower-, mean-, and upper-bound FF parameter sets reported by Vijay et al. [23], together with the optimized FF parameter set proposed in the present study. Although the FF parameter combinations were adopted from Vijay et al. [23], all corresponding slurry densities were calculated independently using the CGMD framework employed in this work. The experimentally measured slurry density of the NMC111 cathode slurry prepared with the same composition as that employed in the CGMD simulations, determined using an Anton Paar Ultrapyc 5000 gas pycnometer, was 1.550 ± 0.002 g cm^{-3} ($n = 3$). Measurement cycles were repeated automatically, with the instrument evaluating repeatability over the three most recent cycles until the variation fell below the selected threshold of 0.1%. This value represents the mean ± standard deviation of three accepted measurement cycles performed on the same sample, rather than three independently prepared samples. This measured density agrees well with the value of 1.550 ± 0.05 g cm^{-3} reported by Rucci et al. [22]. The optimized FF parameter set provides the closest agreement with the experimentally measured slurry density among all parameter combinations considered. However, the selected parameter set was assessed only for the investigated formulation and solid content (NMC111); its transferability to other formulations or solid contents requires additional evaluation.

To assess the contact geometry associated with the density-selected parameter set, normalized overlap distributions were evaluated at timesteps 14 × 10^6, 14.5 × 10^6, and 15 × 10^6. At the final timestep (Table 6), the mean δ/R, with $R = min(R_i, R_j)$, was 0.492 for CBD–CBD contacts, 0.592 for AM–CBD contacts, and 0.321 for AM–AM contacts. The corresponding 95th percentiles were 1.244, 1.266, and 0.557, respectively. These snapshots describe the final portion of the pressure-ramp protocol and are not interpreted as equilibrium overlap distributions.

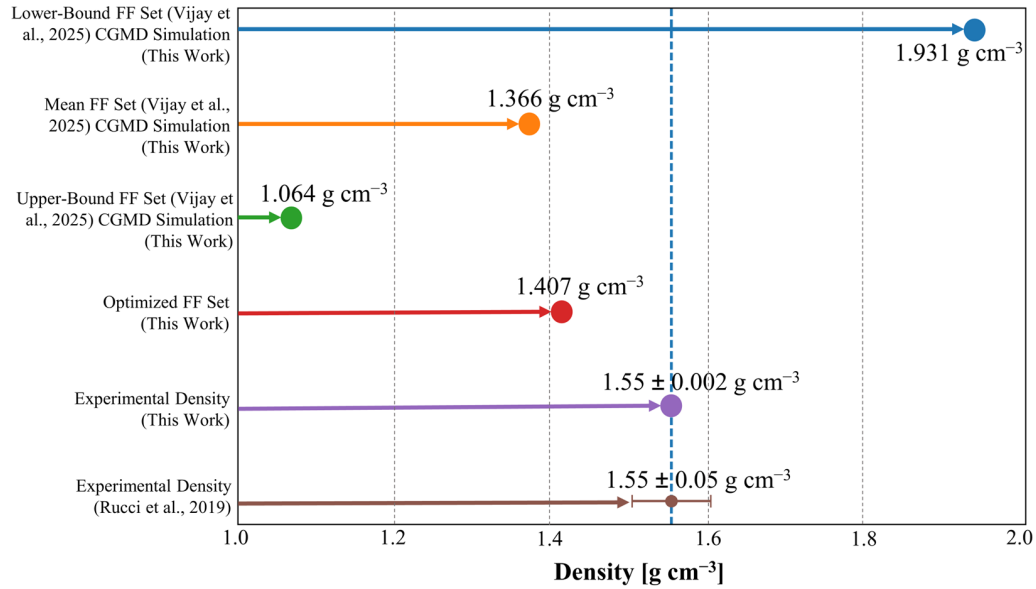


Figure 9. Comparison of slurry densities obtained from CGMD simulations performed in the present study using the lower-, mean-, and upper-bound FF parameter sets adopted from Vijay et al. [23], together with the optimized FF parameter set proposed in this work. The simulated densities are compared with the experimental density measured in the present study and the literature value reported by Rucci et al. [22]. The blue vertical dashed line represents the experimentally measured density of 1.55 g cm^{-3} obtained in this work.

Table 6. Normalized overlap statistics at timestep 15 × 10^6 of the density confirmation simulation. $R = min(R_i, R_j)$. Statistics include contacting pairs only and use the assigned simulation contact radii.

Contact Type	Number of Contacting Pairs	Mean δ/R	Median δ/R	95th Percentile
CBD-CBD	982,539	0.492	0.410	1.244
AM-CBD	17,122	0.592	0.495	1.266
AM-AM	73	0.321	0.339	0.557

The distributions indicate substantial overlap relative to the assigned contact radii. Although CBD particles represent effective solvent-containing domains, this coarse-grained interpretation does not by itself establish the physical adequacy of the observed overlap magnitudes. The results therefore identify contact geometry as an additional model-assessment criterion beyond agreement with bulk density. In particular, changes in the simulated density should be interpreted in terms of the model's represented volume and particle interpenetration, rather than as comparable changes in the intrinsic density of the real slurry.

3.5. Experimental and CGMD Evaluation of Slurry Viscosity

Following density evaluation, the same NMC111 slurry composition was experimentally characterized to establish a rheological reference for the independent assessment of the density-optimized CGMD model. Its experimentally measured density was 1.550 ± 0.002 g cm^{-3}, as discussed in Section 3.4. Rheological measurements were then performed using a Lamy Rheology CP4000 Plus rotational rheometer to establish an experimental reference for the subsequent evaluation of the CGMD model. Figure 10 presents the experimentally measured viscosity and torque responses under constant shear rates of 65, 173, and 500 s^{-1}, together with a shear-rate ramp test from 65 to 500 s^{-1}. At 65 s^{-1}, both viscosity and torque exhibited a pronounced transient decrease, followed by a quasi-steady response, indicating gradual shear-induced rearrangement of the slurry structure. The transient response became considerably less pronounced at higher shear rates. Over the

steady-state evaluation interval, the average viscosities were 10,980 ± 450, 5630 ± 140, and 2900 ± 100 mPa·s at 65, 173, and 500 s^{-1}, respectively. During the shear-rate ramp, the continuous decrease in apparent viscosity confirmed the shear-thinning behavior of the slurry. Viscosity ± values represent signal fluctuations over the 300 s measurement.

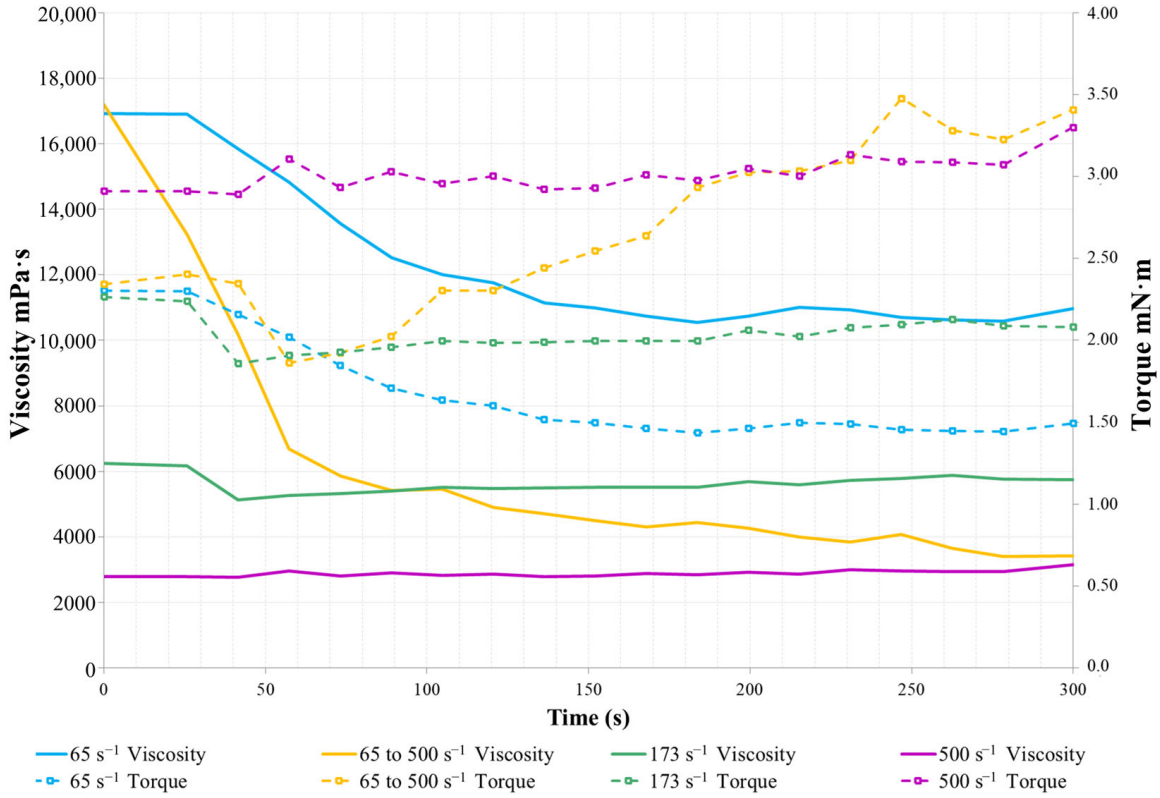


Figure 10. Experimental viscosity and torque responses of the NMC111 slurry measured under constant shear rates of 65, 173, and 500 s^{-1} and during a shear-rate ramp test (65–500 s^{-1}). Solid lines represent the apparent viscosity, whereas dashed lines denote the corresponding torque.

The torque response provides additional insight into the time-dependent rheological behavior of the slurry. Under the constant shear rate of 65 s^{-1}, the torque decreased progressively from approximately 2.30 to 1.45 mN·m during the initial stage and subsequently approached a quasi-steady level. This behavior is consistent with the pronounced decrease in apparent viscosity and may reflect gradual shear-induced rearrangement and partial disruption of the particle–binder microstructure. At this relatively low shear rate, the imposed deformation was insufficient to rapidly disrupt the microstructural network, resulting in a prolonged transient response. At 173 s^{-1}, the torque initially decreased but subsequently stabilized at approximately 2.04 ± 0.05 mN·m over the 100–300 s interval, indicating that a nearly steady flow structure was established after the initial adjustment period. The 500 s^{-1} measurement exhibited the most stable torque response, with an average value of approximately 3.04 ± 0.10 mN·m over the same interval. The comparatively stable viscosity and torque at 500 s^{-1} indicate that a quasi-steady rheological response was reached more rapidly under the higher imposed shear rate. In contrast, the torque was not expected to remain constant during the 65–500 s^{-1} ramp experiment because the applied shear rate continuously increased. The initial decrease followed by a gradual increase in torque reflects the combined effects of shear-induced structural breakdown, which reduces viscosity, and the increasing deformation rate, which raises the required shear stress.

Following the experimental characterization, the optimized FF parameter set presented in Figure 8a was evaluated through viscosity simulations to assess its applicability to another key property of the slurry. The equilibrated mesostructure obtained from the density confirmation simulation in Figure 8b was used directly as the initial configuration, thereby maintaining consistency between the density and viscosity calculations. Since viscosity was not included in the DOE screening or response-optimization procedure, comparison between the experimental and CGMD-derived viscosities provides an independent assessment of the applicability of the selected FF parameter set. As described in Section 2.2.3, the first 10×10^6 timesteps were used exclusively for zero-shear equilibration and were therefore excluded from the viscosity evaluation. Subsequently, simple shear deformation was imposed using the SLLOD algorithm at constant shear rates of 65 and 500 s^{-1} for an additional 20×10^6 timesteps. Figure 11 compares the evolution of the calculated apparent viscosity and the off-diagonal P_{xy} component of the pressure tensor during the NEMD simulations. At a shear rate of 500 s^{-1}, both quantities rapidly reached statistically stationary values after the equilibration stage. The calculated viscosity remained stable throughout the production run, yielding an average value of 2226 ± 23 mPa·s, compared with the experimentally measured value of 2900 ± 100 mPa·s shown in Figure 10. This corresponds to a relative deviation of 23.2%. This deviation exceeds the experimental signal fluctuations (~3.4%), but the separate contributions of force-field limitations, numerical effects, and systematic experimental uncertainty remain unresolved. Because viscosity was not included in the DOE-based parameter-selection procedure, this result provides an independent indication that the selected FF parameters capture the slurry's high-shear rheological response with reasonable accuracy. At 173 s^{-1}, the simulated viscosity also exhibited a comparatively stable response, with an approximate mean of 4696 mPa·s, compared with the experimental value of 5630 ± 140 mPa·s (an approximate relative deviation of 16.6%). The 173 s^{-1} mean is an approximate value and should be confirmed from the underlying numerical data before final submission.

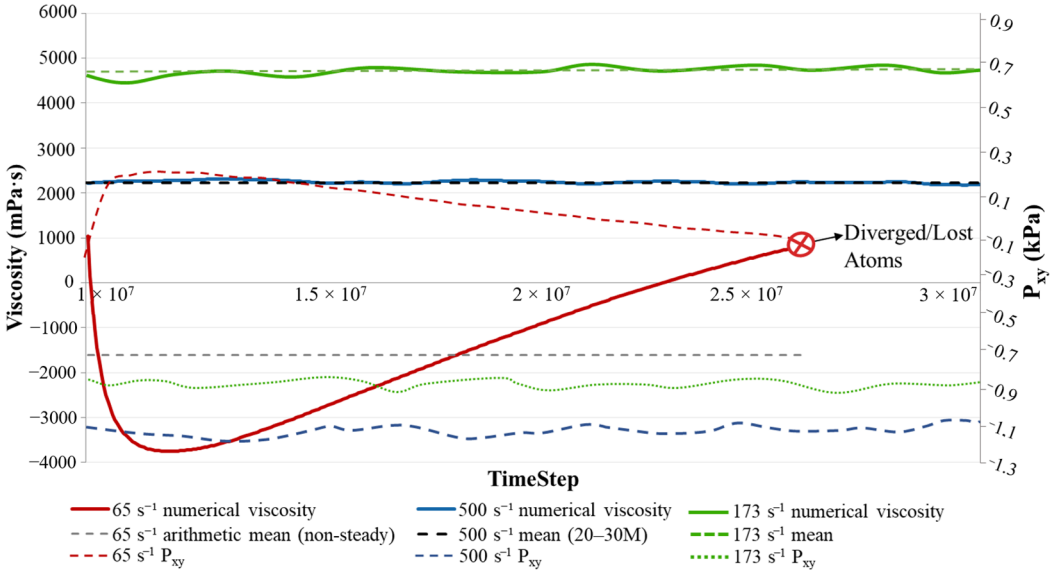


Figure 11. Time evolution of the apparent viscosity and the off-diagonal P_{xy} component of the pressure tensor obtained from the NEMD simulations at constant shear rates of 65, 173 and 500 s^{-1} using the optimized FF parameter set.

Although the same integration timestep and simulation protocol were applied at both shear rates, numerical stability was not maintained at 65 s^{-1}. A systematic timestep-sensitivity analysis was not performed; therefore, the specific contribution of the integration timestep to this instability could not be isolated.

As shown in Figure 11, a different behavior was observed in the NEMD simulation performed at a shear rate of 65 s^{-1}. Under this low-shear condition, the internal stress fluctuations of the system became highly dominant relative to the applied shear stress [26,27]. Consequently, the off-diagonal P_{xy} component of the pressure tensor exhibited a highly unstable trajectory: it initially had a negative value, rapidly increased to a positive peak following the equilibration stage, but then gradually decreased, crossing back into negative values during the production stage. As indicated by Equation (6), this behavior in P_{xy} caused the calculated apparent viscosity to drop to unphysical negative values (reaching a minimum of approximately −3700 mPa·s). Later in the production stage, following a shear-induced box flip (a periodic remapping of the tilted simulation cell) (around timestep 2.6×10^7), approximately 2300 atoms could no longer be remapped to valid positions within the simulation domain, resulting in atom loss and subsequent termination of the NEMD simulation. This behavior was further supported by the total energy response, which exhibited a persistent downward drift at 65 s^{-1}, whereas the total energy at 500 s^{-1} remained bounded within a comparatively stable range, as shown in Figure 12. As illustrated in Figure 12, repeated box flips at 500 s^{-1} did not compromise the numerical stability of the simulation, whereas the first box flip at 65 s^{-1} was followed by atom loss and subsequent simulation divergence. Therefore, this behavior should not be interpreted as an intrinsic rheological response of the slurry, but rather as a numerical instability of the NEMD simulation arising under the applied low-shear condition.

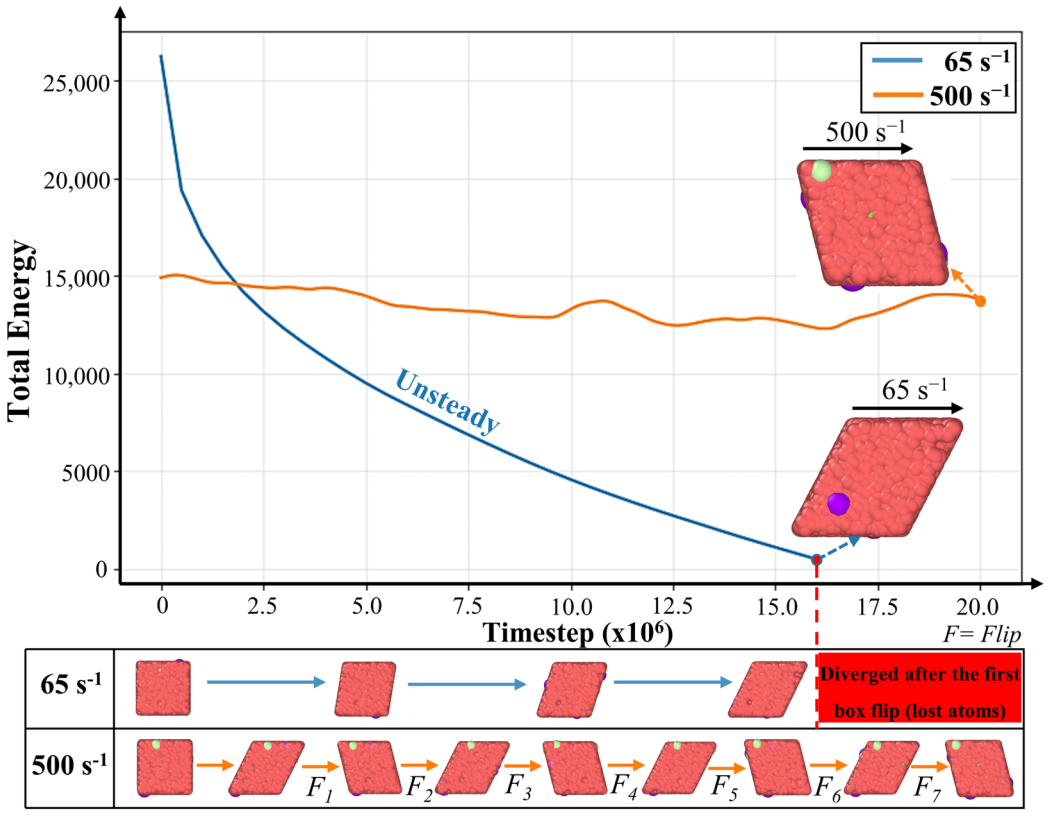


Figure 12. Total-energy evolution during the NEMD simulations at shear rates of 65 and 500 s^{-1}. The 500 s^{-1} simulation remained stable through multiple box flips, whereas the 65 s^{-1} simulation diverged after the first box flip because of atom loss.

Overall, the FF parameter set selected through the density-based DOE workflow provided a reasonably consistent prediction of the experimental viscosity at 500 s^{-1}, with a relative deviation of 23.2%. Since viscosity was not included in the DOE or response-optimization procedure, this comparison constitutes an independent assessment of the selected parameters. At 65 s^{-1}, the low mean P_{xy} signal relative to its temporal fluctuations prevented a stable viscosity estimate. The remaining discrepancy should therefore be interpreted as a limitation of transferring density-calibrated parameters to a different rheological observable; it suggests that additional property-specific or multi-objective calibration may be needed, rather than establishing a universal parameter set.

4. Conclusions

In this study, a CGMD framework coupled with a fractional factorial DOE was employed to systematically investigate the influence of FF parameters on the density of an NMC111 cathode slurry. The investigated formulation had a nominal dry-solid composition of 85 wt% NMC111, 9 wt% Super C65 carbon black, and 6 wt% PVDF, corresponding to an AM/CBD mass ratio of 85/15, at a target slurry solid content of 46 wt%. In the CGMD slurry model, the solvent contribution was incorporated into the effective CBD particles. In this regard, the LJ and GH potentials were employed to described interparticle interactions and contact mechanics. Eight FF parameters (ε_{AM}, σ_{AM}, r_{c_AM}, ε_{CBD}, σ_{CBD}, k_n, γ_n, and X_μ) associated with the LJ and GH formulations were considered, and fractional factorial DOE sets were constructed to evaluate their main effects. Subsequently, the FF parameter set obtained through density-based response optimization was further evaluated through NEMD viscosity simulations together with experimental density and rheological measurements. The main findings of this study are summarized as follows:

- DOE-based sensitivity analysis quantitatively identified the governing FF parameters controlling slurry density. Among the eight investigated parameters, the normal contact elastic constant (k_n) was found to be the dominant parameter, while the AM LJ distance parameter (σ_{AM}) exhibited a secondary contribution.
- The observed dependence of slurry density on k_n was further supported by the equilibrium morphologies, where increasing the normal contact stiffness produced larger equilibrium simulation-box dimensions and lower simulated packing density.
- Increasing σ_{AM} increased the equilibrium particle separation, reduced packing efficiency, and consequently resulted in a lower simulated slurry density.
- CGMD simulations were performed using the lower-bound, mean, and upper-bound FF parameter sets reported in the literature. These parameter sets predicted slurry densities of 1.931, 1.366, and 1.064 g cm^{-3}, respectively, compared with the experimentally measured density of 1.550 ± 0.002 g cm^{-3}, corresponding to relative deviations of 24.6%, 11.9%, and 31.4%, respectively.
- Density-based response optimization produced a density-optimized FF parameter set, and the corresponding confirmation simulation predicted a slurry density of 1.407 g cm^{-3}, compared with the experimentally measured density of 1.550 ± 0.002 g cm^{-3}, corresponding to a relative deviation of 9.23%. Unlike the lower-, mean-, and upper-bound parameter sets adopted directly from [23], the proposed force-field parameter set was obtained through systematic DOE-based sensitivity analysis and subsequent optimization targeting the experimentally measured density of the investigated slurry. The significance of the resulting 9.23% density deviation, compared with 11.9% for the literature mean parameter set, lies primarily in the systematic, composition-specific parameter selection procedure rather than in the magnitude of the improvement alone. Further independent simulations are required to assess the robustness and transferability of the optimized parameter set.

- The optimized FF parameter set was further assessed through NEMD viscosity simulations without including viscosity in the optimization objective. Experimentally, viscosities of 10,980 ± 450, 5630 ± 140, and 2900 ± 100 mPa·s were measured at shear rates of 65, 173, and 500 s^{-1}, respectively. At 500 s^{-1}, the simulation predicted 2226 ± 23 mPa·s, corresponding to a 23.2% deviation from experiment, demonstrating that the density-selected FF parameter set showed reasonable applicability to an independent rheological response. At the low shear rates 65 s^{-1}, numerical instability associated with box flipping and atom loss prevented reliable viscosity prediction. The 23.2% viscosity deviation at 500 s^{-1} (and approximately 16.6% at 173 s^{-1}) is reported without viscosity-specific readjustment of the density-optimized parameters. These cross-property tests indicate that agreement with density alone does not ensure equally close agreement with viscosity, motivating future multi-property calibration.

Author Contributions: Conceptualization, M.G. and E.B.; methodology, M.G. and E.B.; software, M.G.; formal analysis, M.G.; investigation, M.G.; writing—original draft preparation, M.G.; writing—review and editing, E.B.; visualization, M.G.; supervision, E.B.; funding acquisition, E.B. All authors have read and agreed to the published version of the manuscript.

Funding: The article processing charge (APC) was funded by the BATTwin project ("Flexible and scalable digital-twin platform for enhanced production efficiency and yield in battery cell production lines"), supported by the European Union's Horizon Europe programme under grant agreement No. 101137954.

Data Availability Statement: The data presented in this study are available within the article.

Acknowledgments: This project has received funding from the European Union's Horizon Europe programme under grant agreement No. 101137954. The authors would like to thank the rest of the BATTwin consortium for supporting this research. The numerical calculations reported in this paper were partially performed at TUBITAK ULAKBIM, High Performance and Grid Computing Center (TRUBA resources). During the preparation of this work, the authors used GPT-5.5 to improve the language and readability of the manuscript. After using this tool/service, the authors reviewed and edited the content as needed and take full responsibility for the content of the published article.

Conflicts of Interest: The authors declare no conflict of interest also the funder was not involved in the study design; data collection, analysis, or interpretation; the writing of the article; or the decision to submit for publication.

Abbreviations

The following abbreviations are used in this manuscript:

AM	Active material
ANOVA	Analysis of variance
CBD	Carbon–binder domain
CGMD	Coarse-grained molecular dynamics
DOE	Design of experiments
FF	Force field
GH	Granular Hertz
LAMMPS	Large-scale Atomic/Molecular Massively Parallel Simulator
LIB	Li-ion battery
LJ	Lennard-Jones
LJ/SF	Shifted-force Lennard-Jones
NEMD	Non-equilibrium molecular dynamics
NMC111	$LiNi_{1/3}Mn_{1/3}Co_{1/3}O_2$
NMP	N-methyl-2-pyrrolidone
NPT	Constant particle number, pressure, and temperature
PVDF	Polyvinylidene fluoride

SC	Solid content
SEM	Scanning electron microscopy

References

1. Ngoy, K.R.; Lukong, V.T.; Yoro, K.O.; Makambo, J.B.; Chukwuati, N.C.; Ibegbulam, C.; Eterigho-Ikelegbe, O.; Ukoba, K.; Jen, T.C. Lithium-ion batteries and the future of sustainable energy: A comprehensive review. *Renew. Sustain. Energy Rev.* **2025**, *223*, 115971. [CrossRef]
2. Takami, N.; Ise, K.; Harada, Y.; Iwasaki, T.; Kishi, T.; Hoshina, K. High-energy, fast-charging, long-life lithium-ion batteries using TiNb2O7 anodes for automotive applications. *J. Power Sources* **2018**, *396*, 429–436. [CrossRef]
3. Bandara, T.G.T.A.; Viera, J.C.; González, M. The next generation of fast charging methods for Lithium-ion batteries: The natural current-absorption methods. *Renew. Sustain. Energy Rev.* **2022**, *162*, 112338. [CrossRef]
4. Patnaik, S. Overview of electrode advances in commercial Li-ion batteries. *Ionics* **2024**, *30*, 3069–3090. [CrossRef]
5. Lei, Y.; Xu, L.; Chan, Q.N.; Li, A.; Yin Yuen, A.C.; Yuan, Y.; Yeoh, G.H.; Wang, W. Recent advances in separator design for lithium metal batteries without dendrite formation: Implications for electric vehicles. *eTransportation* **2024**, *20*, 100330. [CrossRef]
6. Kainat, S.; Anwer, J.; Hamid, A.; Gull, N.; Khan, S.M. Electrolytes in Lithium-Ion Batteries: Advancements in the Era of Twenties (2020's). *Mater. Chem. Phys.* **2024**, *313*, 128796. [CrossRef]
7. Chouchane, M.; Rucci, A.; Lombardo, T.; Ngandjong, A.C.; Franco, A.A. Lithium ion battery electrodes predicted from manufacturing simulations: Assessing the impact of the carbon-binder spatial location on the electrochemical performance. *J. Power Sources* **2019**, *444*, 227285. [CrossRef]
8. Lee, S.; Sastry, A.M.; Park, J. Study on microstructures of electrodes in lithium-ion batteries using variational multi-scale enrichment. *J. Power Sources* **2016**, *315*, 96–110. [CrossRef]
9. Manoharan, A.; Chong, J.J.; Choong, Z.J.; Lambert, S.; Kumar Gupta, R.; Chandra, D.; Jain, A.; Rao, A.; Sharma, A. Optimizing lithium-ion battery manufacturing with digitalization and AI-driven frameworks. *Int. J. Adv. Manuf. Technol.* **2026**, *142*, 1–37. [CrossRef]
10. Trembacki, B.L.; Noble, D.R.; Brunini, V.E.; Ferraro, M.E.; Roberts, S.A. Mesoscale Effective Property Simulations Incorporating Conductive Binder. *J. Electrochem. Soc.* **2017**, *164*, E3613. [CrossRef]
11. Mistry, A.N.; Smith, K.; Mukherjee, P.P. Secondary-Phase Stochastics in Lithium-Ion Battery Electrodes. *ACS Appl. Mater. Interfaces* **2018**, *10*, 6317–6326. [CrossRef] [PubMed]
12. Stephenson, D.E.; Walker, B.C.; Skelton, C.B.; Gorzkowski, E.P.; Rowenhorst, D.J.; Wheeler, D.R. Modeling 3D Microstructure and Ion Transport in Porous Li-Ion Battery Electrodes. *J. Electrochem. Soc.* **2011**, *158*, A781. [CrossRef]
13. Forouzan, M.M.; Chien, C.W.; Bustamante, D.; Lange, W.; Mazzeo, B.A.; Wheeler, D. Predictive Particle-Based Simulation of the Fabrication of Li-Ion Battery Electrodes. *ECS Meet. Abstr.* **2015**, *227*, 1798. [CrossRef]
14. Thompson, A.P.; Aktulga, H.M.; Berger, R.; Bolintineanu, D.S.; Brown, W.M.; Crozier, P.S.; in't Veld, P.J.; Kohlmeyer, A.; Moore, S.G.; Nguyen, T.D.; et al. LAMMPS—A flexible simulation tool for particle-based materials modeling at the atomic, meso, and continuum scales. *Comput. Phys. Commun.* **2022**, *271*, 108171. [CrossRef]
15. Yao, X.; Hafiz, H.; Chen, L.; Cai, W.; Mao, Z.; Hu, S. Coarse-grained molecular dynamics modelling of lithium-ion battery electrode drying: A sensitivity analysis. *J. Manuf. Process.* **2025**, *144*, 54–59. [CrossRef]
16. Lombardo, T.; Hoock, J.B.; Primo, E.N.; Ngandjong, A.C.; Duquesnoy, M.; Franco, A.A. Accelerated Optimization Methods for Force-Field Parametrization in Battery Electrode Manufacturing Modeling. *Batter. Supercaps* **2020**, *3*, 721–730. [CrossRef]
17. Forouzan, M.M.; Chao, C.W.; Bustamante, D.; Mazzeo, B.A.; Wheeler, D.R. Experiment and simulation of the fabrication process of lithium-ion battery cathodes for determining microstructure and mechanical properties. *J. Power Sources* **2016**, *312*, 172–183. [CrossRef]
18. Ngandjong, A.C.; Rucci, A.; Maiza, M.; Shukla, G.; Vazquez-Arenas, J.; Franco, A.A. Multiscale Simulation Platform Linking Lithium Ion Battery Electrode Fabrication Process with Performance at the Cell Level. *J. Phys. Chem. Lett.* **2017**, *8*, 5966–5972. [CrossRef] [PubMed]
19. Lombardo, T.; Ngandjong, A.C.; Belhcen, A.; Franco, A.A. Carbon-Binder Migration: A Three-Dimensional Drying Model for Lithium-ion Battery Electrodes. *Energy Storage Mater.* **2021**, *43*, 337–347. [CrossRef]
20. Ngandjong, A.C.; Lombardo, T.; Primo, E.N.; Chouchane, M.; Shodiev, A.; Arcelus, O.; Franco, A.A. Investigating electrode calendering and its impact on electrochemical performance by means of a new discrete element method model: Towards a digital twin of Li-Ion battery manufacturing. *J. Power Sources* **2021**, *485*, 229320. [CrossRef]
21. Yao, X.; Xiao, Y.; Wang, Z.; Zhang, Z.; Cai, W.; Zeng, Y.; Chen, L. Coarse-grained molecular dynamics simulations of microstructure evolution and debonding in water-based cathode electrode drying. *J. Mater. Process. Technol.* **2023**, *321*, 118154. [CrossRef]
22. Rucci, A.; Ngandjong, A.C.; Primo, E.N.; Maiza, M.; Franco, A.A. Tracking variabilities in the simulation of Lithium Ion Battery electrode fabrication and its impact on electrochemical performance. *Electrochim. Acta* **2019**, *312*, 168–178. [CrossRef]

23. Vijay, U.; Galvez-Aranda, D.E.; Zanotto, F.M.; Le-Dinh, T.; Alabdali, M.; Asch, M.; Franco, A.A. A hybrid modelling approach coupling physics-based simulation and deep learning for battery electrode manufacturing simulations. *Energy Storage Mater.* **2025**, *75*, 103883. [CrossRef]
24. Meibodi, M.E.; Vafaie-Sefti, M.; Rashidi, A.M.; Amrollahi, A.; Tabasi, M.; Kalal, H.S. The role of different parameters on the stability and thermal conductivity of carbon nanotube/water nanofluids. *Int. Commun. Heat Mass Transf.* **2010**, *37*, 319–323. [CrossRef]
25. Luding, S. Introduction to discrete element methods. *Eur. J. Environ. Civ. Eng.* **2008**, *12*, 785–826. [CrossRef]
26. Lin, L.; Kedzierski, M.A. Density and viscosity of a polyol ester lubricant: Measurement and molecular dynamics simulation. *Int. J. Refrig.* **2020**, *118*, 188–201. [CrossRef] [PubMed]
27. Peng, Y.; Yue, T.; Li, S.; Gao, K.; Wang, Y.; Li, Z.; Ye, X.; Zhang, L.; Liu, J. Rheological and structural properties of associated polymer networks studied via non-equilibrium molecular dynamics simulation. *Mol. Syst. Des. Eng.* **2021**, *6*, 461–475. [CrossRef]

Disclaimer/Publisher's Note: The statements, opinions and data contained in all publications are solely those of the individual author(s) and contributor(s) and not of MDPI and/or the editor(s). MDPI and/or the editor(s) disclaim responsibility for any injury to people or property resulting from any ideas, methods, instructions or products referred to in the content.